Penta-SiCN: A Highly Auxetic Monolayer

Shambhu Bhandari Sharma,*,† Issam A. Qattan,*,† Meghnath Jaishi,‡ and Durga Paudyal¶

†*Khalifa University of Science and Technology, Department of Physics, P.O. Box 127788, Abu Dhabi, United Arab Emirates*
‡*Mechanical Engineering Department, University of Louisville, Louisville, KY, USA*
¶*Ames Laboratory, Iowa State University, Ames, IA 50011, USA*

E-mail: CorresspondingAuthors*:shambhu.sharma@ku.ac.ae; issam.qattan@ku.ac.ae

Abstract

The negative Poisson's (NPR) ratio in a two-dimensional (2D) material is a counterintuitive mechanical property that facilitates the development of nanoscale devices with sophisticated functionality. Inspired by the peculiar buckled lower-symmetric, trilayered geometry of pentagonal monolayers, we theoretically predict penta-SiCN, a ternary auxetic metallic monolayer with highly tunable NPR. The penta-SiCN is structurally, thermally, dynamically, and mechanically stable, and sustainable at and beyond room temperature with experimental feasibility. It possesses non-trivial geometrical and mechanical isotropy and relatively moderate thickness. Remarkably, the shorter and quasi sp^3-hybridized C−N bond and the rigidity against the strain allow the monolayer to possess a high value of NPR (-0.136), even higher than that of black phosphorene, extendable up to -0.639 by 4% of biaxial stretching. On the other hand, the 2D Young's modulus of 129.88 N/m decreases to 41.34 N/m at equivalent stretching, indicating relative softening and flexibility. Interestingly, a buckled−to−planar phase transition is identified at 10% biaxial strain before it suffers the fracture at 16%. Additionally, the strong optical anisotropy, absorbance (up to 6.51×10^5 cm^{-1}), and presence of plasmon frequency demonstrate its potential application in optomechanical and plasmonics.

Keywords: Density Functional Theory, penta-SiCN, Negative Poisson's ratio, mechanical properties, strains effect, electronic properties, optical properties.

INTRODUCTION

Moving beyond the conventional hexagonal honeycomb two-dimensional (2D) structure, the theoretical prediction of Cairo pentagraphene[1] surged an interest in pentagonal isostructures due to their extraordinary mechanical and optoelectronic properties[2–5]. In particular, the presence of the negative Poisson's ratio (NPR) in penta-graphene[1] sheds new light on pentagonal monolayer for advanced mechanical properties. The NPR materials, so−called auxetic or mechanical metamaterials, have the tendency to shrink (expand) laterally when compressed (stretched) axially. Most of these materials manifest NPR ranging from -1 to 0. They have higher indentation, impact, and crack propagation resistance with superior sound absorption performance[6,7]. In addition, when subjected to out-of-plane bending moments, the NPR material transforms to a dome-shaped structure as compared to the saddle-shaped structure exhibited by positive Poisson's ratio (PPR) materials[8]. These excellent properties allow NPR materials to have broad applications in the automotive, aerospace, marine and other industrial fields[9]. Furthermore, the novel auxetic

structural behaviour, and the associated electronic and optical properties offer an extensive potential in advanced applications such as sensors, biomedicine, fasteners, bullet-proof sheilds, sports equipments, tissue engineering, and futuristic devices[10–15].

The foraging of auxetic materials have mainly enthralled on bulk systems at early stages, the theoretical and experimental evidences of existence of first intrinsic NPR 2D material in 2014, the black phosphorene(-0.027)[16], triggered the research interest on low-dimensional materials. Since then, NPR is only reported theoretically but not experimentally in several 2D materials[17] including borophane (-0.053)[18], BP_5 (-0.037)[19], TiN[20], Be_2C (-0.566)[21], 2D Be_5C_2 (-0.041)[22], penta-B_2N_4 (-0.02) and penta-BN_2 (-0.19)[23], penta-graphene (-0.07)[1], and penta-$PdSe_2$ (-0.022)[24], which are still relatively smaller family in the vast ocean of 2D materials. The current experimental efforts to synthesis 2D auxetic materials are premature and lagging behind the theoretical studies, as there have been no direct experimental evidence of NPRs. However, an indirect experimental evidence of NPR is reported in black phosphorene by employing Raman spectroscopy. Clearly, such 2D auxetic materials are fascinating and desirable once experimentally synthesized.

Particularly, the pentagonal monolayers are drawing considerable attention in auxetic nanomaterials research due to their unique non-planar geometry[1,23,24]. When strained longitudinally, their 4-irregular pentagonal Cairo tile structure with low symmetry and trilayered geometry creates high chances of lateral atomic moments demonstrating the NPR effects. Previous studies on buckled and puckered structures have also reported higher NPR as compared to their planar counterpart[15,17]. Additionally, most of these reported auxetic 2D materials show invariable intrinsic Poissons ratio[15]. What is lacking here is the tunability of NPR creating the enormous potential of electromechanical devices for various industrial fields, including medicine, defense, and portable electronics. Therefore, it is desirable to go one step further to obtain the essential understanding of the influence of strain on NPR. Such tunable NPR 2D materials offer promising opportunities for smart device designs[15]. Similarly, penta monolayer inherits the robust band topology, and visible light harvesting direct-bandgap semiconducting to metallic electronic behavior, which are reported to be highly demanding in cutting edge technological devices such as optomechanical sensors, lithium-ion batteries, and solar cells[25]. Hence, understanding electronic behavior, and light-matter interacting optical response are crucial for their applicability.

The quest for a new stable and experimentally feasible auxetic material is always very exciting in materials science. Particulary, the ternary penta-sheet is of current interest due to their intriguing physical and chemical properties, and potential pertinency[26]. Expanding the family of ternary 2D pentagonal monolayers, in this work, we have theoretically identified and predicted the very first ternary metallic and highly auxetic pentagonal silicon carbon nitride (p-SiCN). Such material is highly promising due to its unique physical and chemical properties, which have not been explored before in ternary penta monolayers. The stability and experimental feasibility of the monolayer are tested by calculating and analyzing the chemical, structural, thermal, mechanical, and dynamical features and parameters. The presence of NPR, 2D Young's modulus, and the ultimate strength along with their criteria and shreds of evidence are examined by the variation of bond length and strain energy with applied strain. Additionally, the strong anisotropic optical absorbance and presence of plasmon frequency are identified and demonstrated, which are crucial for optomechanical and plasmonics device applications.

RESULTS AND DISCUSSION

A. Structural properties

The geometrical structure of p-SiCN is modeled by replacing 4-coordinated and 3-coordinated carbon atoms with silicon and nitrogen from the optimized parent penta-graphene. A unit cell consisting of 2Si, 2C, and 2N atoms, a tri-

layered structure, is fully relaxed to achieve the lowest energy and atomic forces. The fully relaxed configuration has Si sublattices at the middle layer and N (C) and C (N) sublattices at the top and bottom layers. The structure retains the pentagonal symmetry belonging to P-421m symmetry (space group No. 113). The monolayer has a tetragonal lattice with a lattice parameter a=b=4.31 Å (a=b=4.28 Å from plane-wave approach), is unique from other ternary pentagonal isostructures. Expanding the unit cell into a larger supercell, one can see four distinct irregular pentagonal Cairo tiles (labeled by 1 to 4 in Figure 1a) which preserves the periodic boundary conditions (Figure 1a). In the primitive cell, the two C atoms have slightly different bond distances with a Si atom, we consider these atoms as C1 and C2 to remove the obscure visualization. The justification for this choice is provided later while explaining mechanical behavior. The stable structure of p-SiCN has Si−N, C−N and Si−C1, and Si−C2 bond lengths of 1.83, 1.38, 1.85, and 1.86 Å, respectively.

Remarkably, the centrosymmetric quasi sp^3-hybridized C−N bond is shorter in p-SiCN than that of the hexagonal sp^2-hybridized C_3N (1.40Å)[27]. This uniquely shorter bond length foresight the strength and stability of the monolayer. Similarly, the thickness of the monolayer (h), calculated by measuring differences between the vertical extremities of atoms, is 1.24 Å, which is equivalent to the penta- graphene (1.20 Å)[1] contrasting with those of penta-BP_5 (2.50 Å)[28] and penta-CN_2 (1.52 Å)[29]. Additionally, the accounted bond angles of Si−C2−N (α), C1−Si−C2 (β), and C2−N−Si (γ) are 118.7°, 41.7°, and 114.8°, respectively.

To further corroborate the chemical stability, the computed chemical charge density is visualized in Figure 1b. The sharing of equal and unequal electronic charges leading to covalent and ionic bonds are represented by dumbbell and concentric contour lines, respectively. The intensity of the higher value of charge density region is displayed by pink color code (Figure 1b). Only the C−N is covalent, whereas Si−N, Si−C1, and Si−C2 are ionic.

The negative cohesive (-4.36 eV/atom) and formation (-1.11 eV/atom) energies ensure the stability and experimental feasibility/synthesis of the p-SiCN monolayer. The presence of only real phonon dispersion in both equilibrium and tensile strained conditions (upto 10%) in the entire Brillouin Zone confirms the dynamical stability of the monolayer. However, a minimal imaginary dispersion is observed at -4% bi-axial strain, which indicates dynamical unstability against compression. (Figure 1d-f). The 3 acoustic and 15 optical branches with high vibration frequencies comparable to penta graphene[1] and graphene[30,31] indicate the relative dynamical stability. To further corroborate, we investigate the thermal stability of p-SiCN by performing *ab-initio* molecular dynamics (AIMD) simulations from (300−1000)K each with a time step of 1 fs (Figure 1c). At 300 K, AIMD calculations show that the the structure remains intact without suffering any significant distortion. Similarly, a slight difference in the total potential energy around a constant value is detected at 1000 K, which concludes that the penta-SiCN is thermally stable even at high temperatures.

B. Mechanical properties

To test the machinability, device fabrication and operation of p-SiCN, mechanical stability and strength are investigated. The relevant second-order elastic constants (C_{ij}) are computed using the strain-energy method[32]. The computed values of C_{11}, C_{22}, C_{12} and C_{66} are 132.16, 133.59, -17.44, and 74.80 N/m, respectively. The fulfillment of mechanical stability criteria[33], $C_{11}C_{22} - {C_{11}}^2 > 0$, and $C_{66} > 0$ ensures the mechanical stability of p-SiCN. The 2D Young's modulus in two crystallographic (100) and (010) directions, $Y_a = (C_{11}^2 - C_{12}^2)/C_{11}$ and $Y_b = (C_{22}^2 - C_{12}^2)/C_{11}$, are 129.88 and 131.29 N/m, respectively. These values suggest that p-SiCN is relatively softer than other ternary penta monolayers, however, it is equivalently stiffer to binary penta monolayers and hexagonal transition metal dichalcogenides (Table 1). Similarly, the Poisson's ratios in these directions (ν_a=C_{12}/C_{11} and ν_b=C_{12}/C_{22}) are -0.131 and -0.132, respec-

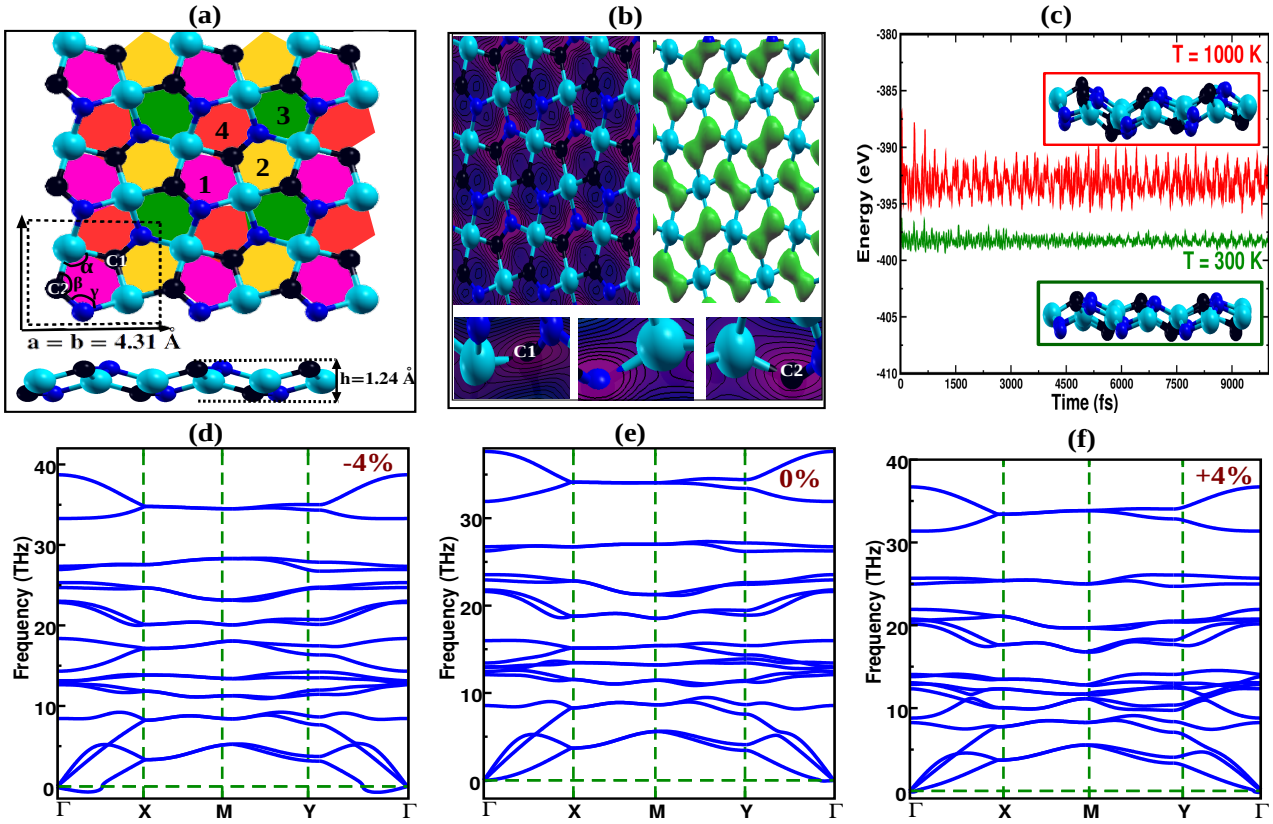

Figure 1: (Color online) (a) Optimized p-SiCN monolayer ($4 \times 4 \times 1$ supercell), cyan, black and blue balls represent Si, C and N atoms, respectively, (b) charge density contour plots, (c) AIMD simulation for the energy fluctuation at T=300 K and T=1000K, with final structures (inset), and (d-f) phonon dispersions at -4%, 0% and +4% biaxial strain, respectively.

tively. The similarity in mechanical properties in different orientations indicate a mechanical isotropy of p-SiCN which is further verified by the perfect circles in polar plots (Figure 4).

The notable NPR in p-SiCN is verified using Refs.[1,34] methodology by applying tensile strain in the x-direction (ε_x = 4%, 6%, and 8%) and observing the lateral response in the y-direction (ε_y). In all cases, the expansion of equilibrium lattice constant in the y-direction ensures the presence of NPR (Figure 2). Even though the continuum mechanics theory is incapable of predicting the presence of NPR in 2D elastic materials[1], our first-principles prediction of NPR in p-SiCN is a rare find. This exceptional NPR result in p-SiCN is attributed to the buckled and asymmetric geometrical structure, particularly, the shorter and quasi sp^3 - hybridized CN bond and the rigidity against the strain (discussed below). This exciting discovery makes the monolayer a superior candidate material for multiple applications such as a tension activatable substrate, a nano-auxetic, and a deformable variable stiffness device.

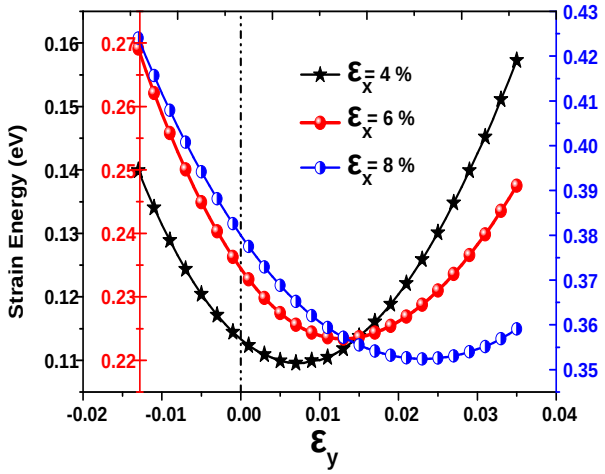

Figure 2: (Color online) NPR verification – Strain energy as a function of uniaxial strain along the y-axis (ε_y) with respective constant uniaxial strains of 4%-black, 6%-red, and 8%-blue along the x-axis (ε_x).

Table 1: The elastic constants $C_{ij=1,2,6}$ (N/m), 2D Young's modulus $Y_{a/b}$ (N/m), Poisson's ratio $\nu_{a/b}$ from this work, and for p-BCN, and p-CNP monolayers.

Materials	Ref	C_{11}	C_{22}	C_{12}	C_{66}	Y_a	Y_b	ν_a	ν_b
p-SiCN	This work	132.15	133.59	-17.44	74.80	129.88	131.29	-0.131	-0.132
p-BCN	Ref.[35]	210.15	170.77	4.27	102.93	210.05	170.66	0.020	0.025
	Ref.[36]	214.45	176.10	4.38	103.54	214.36	175.99	0.020	0.025
	Ref.[32]	223.56	189.16	4.90	104.80	223.45	189.03	0.022	0.026
p-CNP	Ref.[37]	173.32	183.57	4.52	99.01	172	190	-	-

Since strain is unavoidable during the fabrication and machination of layered materials, it is crucial to test the mechanical response against different modes of strain. The response of Young's modulus and Poisson's ratio under biaxial strain is also crucial in the study of the piezoelectric property of materials[38]. Keeping that in mind, we introduce the equi-biaxial strain (ε_{xy}) within a mechanically stable region ($\pm$ 4%) allowing full relaxation of atoms (relaxed−ion). The mechanical parameters, stability, and anisotropy are analyzed. Compressing the monolayer up to 4%, the Young's modulus (NPR) increases (decreases) monotonically up to 145 N/m (0.05), indicating the growth stiffness of p-SiCN. In addition, the mechanical isotropy is maintained throughout the compression except at 2% (Figure 4a). On the other hand, stretching the monolayer, Young's modulus (NPR) decreases (increases) drastically. Just at ε_{xy} = 2%, the Young's modulus (NPR) decreases (increases) exponentially reaching an approximate value of 101 N/m (-0.26). At ε_{xy} = 4%, the Young's modulus (NPR) decreases (increases) reaching a value of 42 N/m (-0.64). Thus, the highly tunable NPR and Young's modulus of p-SiCN monolayer create the enormous potential of electromechanical devices for various industrial fields, including medicine, defense, and portable and flexible electronic devices[15,17].

Besides the Poisson's ratio and Young's modulus, the ultimate strength is an important mechanical property of a nanomaterial. To investigate the elastic-plastic region, ultimate strength and possible reconstruction at higher-order are studied for both uniaxial (ε_x) and biaxial strains (ε_{xy}). The tensile strain is loaded until the monolayer shows bond breaking. The variation of stress, strain-energy and bond length as a function of strain is demonstrated in Figure 5. Remarkably, at ε_{xy} = 10%, all the atoms maintain to lie at the same plane attributing a "buckled to planer" phase transition (Figure 3) with positive phonon frequencies for dynamical stability. This result attracts in-depth research studies and their disruptive applications. It is worth mentioning that a similar phase transition was reported in penta-B_2C monolayer at ε_{xy} =15%, without revealing its dynamical stability[39].

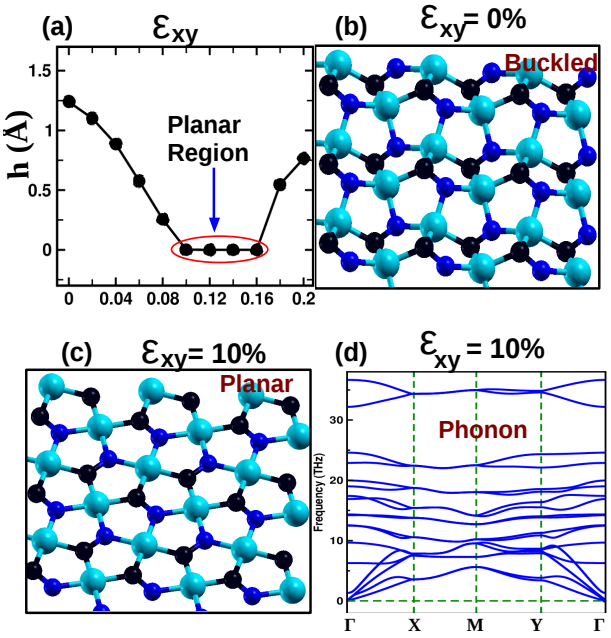

Figure 3: (Color online) Buckled to planner phase transition in p-SiCN. (a) Variation of monolayer thickness with ε_{xy} – red circle encloses the minimum thickness (≈0) from 10% to 16%, (b) buckled p-SiCN with no strain, (c) planar p-SiCN at 10% strain, and (d) phonon dispersions at 10% strain.

Further, there is a sudden drop of stress beyond the critical strain (ε_c) of 16% for both

modes of strain; the continuous growth of strain energy suggests the possibilities of geometrical reconstruction. This value of ε_c is comparable to the p-BCN including many well-known 2D materials. The critical strength for biaxial (U_{bi}) and uniaxial (U_{uni}) strains are 12.14 and 7.99 N/m, respectively, which are lower than that of graphene (34 N/m) and phosphorene (16 N/m). This is also realized by analyzing the variation of bond length of the monolayer with strain (Figure 5). The unusually higher value of U_{bi} as compared to U_{uni} for p-SiCN is linked with the relative phase transition and a higher degree of freedom due to stretching as demonstrated by bond length variation (Figure 5a). For ε_{xy}, the bond lengths increase monotonically up to ε_c except for the rigid and short C−N bond. The thickness decreases and becomes ≈ 0 in the range $10\% \leq \varepsilon_{xy} \leq 16\%$ displaying the planar geometry of the monolayer as mentioned above. On the other end, for ε_x, the Si−C1 (Si−N) increases (decreases) monotonically up to ε_c except for the rigid bonds C−N and Si−C2. Similarly, the thickness of the monolayer decreases continuously up to and beyond $\varepsilon_x = 16\%$ ruling out the presence of phase transition for the uniaxial strain. This indeed further demonstrates the attribution of the NPR effect in p-SiCN.

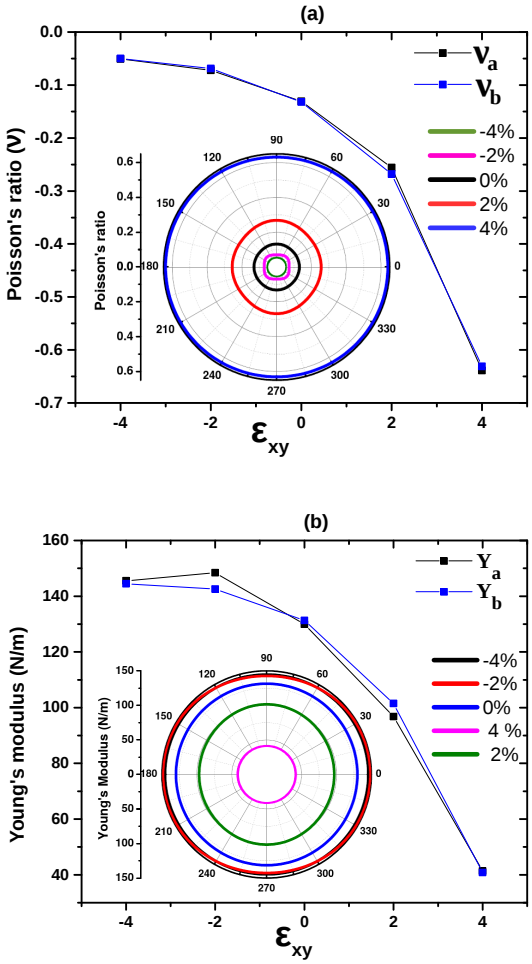

Figure 4: (Color online) The variation of the (a) Poisson's ratio and (b) Young's modulus against biaxial strain loading. The inset describes the orientation dependency.

C. Electronic properties

To probe the electronic properties of p-SiCN, electronic band structure calculations (Figure 6) are performed along the Γ − X − M −Y − Γ high-symmetry directions. Partial density states (PDOS) enrich the understanding of the individual electronic orbital contribution (Figure 7). Both spin-up and spin-down states are degenerate throughout the Brillouin zone, and thus, the structure does not exhibit any spin polarization in its ground state, concluding the non-magnetic behavior of p-SiCN. The absence of bandgap demonstrates the metallic behavior, the first metallic ternary pentagonal monolayer. Interestingly, the valence band and conduction band entwined at the Fermi level at X - M path creating the metallicity. Additionally, a peculiar flat band is observed along the same path at 4 eV. This metallicity is tested against applied strain and electric field. In both cases, the metallic behavior is preserved. The PDOS elucidates the contribution of p-orbitals of C, N, and Si atoms (sp^3 -hybridized) at the vicinity of the Fermi level. However, there is a minor contribution of s-orbital at the same range. This indeed allows us to distinguish it from other ternary penta monolayers[1,2,32,35,37]. Also, the peculiar metallicity renders its application in a desirable electrode material for high-performance lithium-ion batteries and high-quality electronic devices[40].

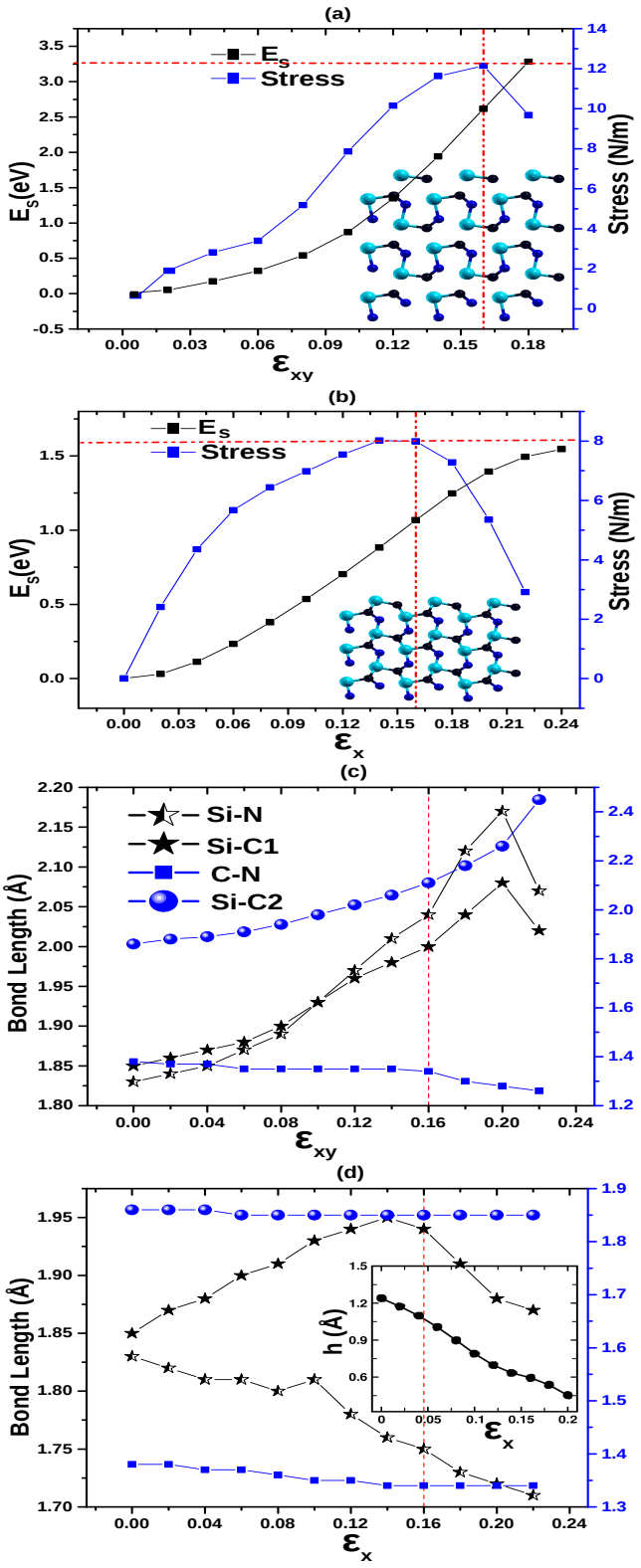

Figure 5: (Color online) Stress and strain energies as a function of (a) biaxial and (b) uniaxial strains. The deformed structures beyond ε_c (dashed red line) are also visualized. The variation of bond lengths with (c) biaxial and (d) uniaxial strains. The variation of monolayer thickness is shown in the inset of (d).

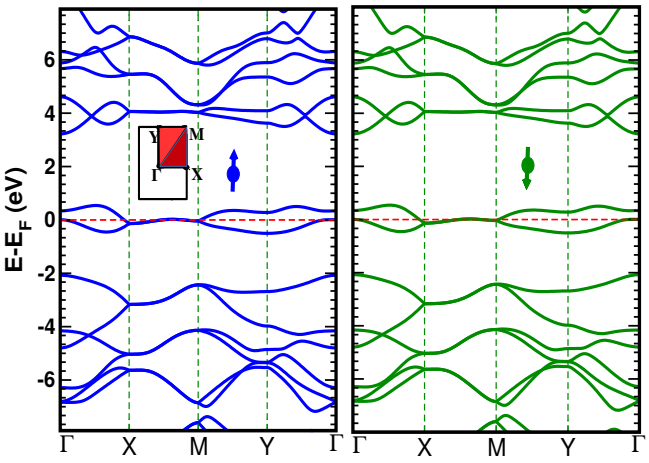

Figure 6: (Color online) Electronic bands spin-up(blue) and spin-down (green) of p-SiCN. Inset shows the first Brillouin zone of the monolayer with high-symmetry lines.

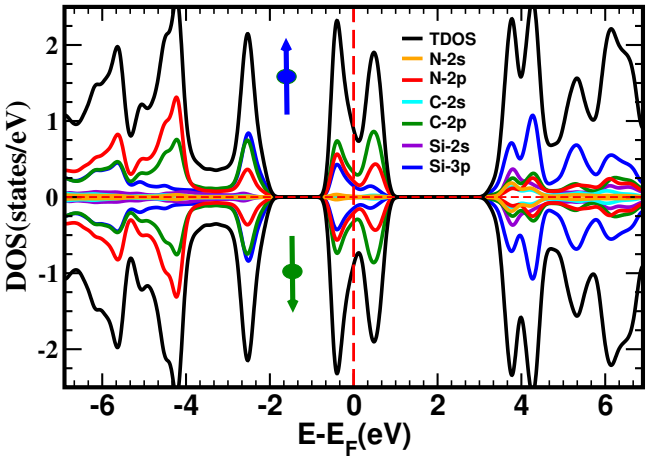

Figure 7: (Color online) The total density of states (TDOS) and partial density of states (PDOS) for spin-up and spin-down.

D. Optical properties

Typically in metals, light interacts with electrons of both valence and conduction bands potentially causing optical activity. SIESTA has been successful in describing the optical sensitivity of low-dimensional materials[35,41,42], the optical response of p-SiCN upon the incidence of an electric field in in-plane (E||x) and out-of-the plane (E||z) direction within the infrared (0−1.62 eV), visible (1.6−3.21 eV), and ultraviolet (3.2 −10 eV) regions are investigated by calculating important optical parameters (Figure 8(a-f)). The dominance of optical spectra in E||x over the E||z orientation shows the strong

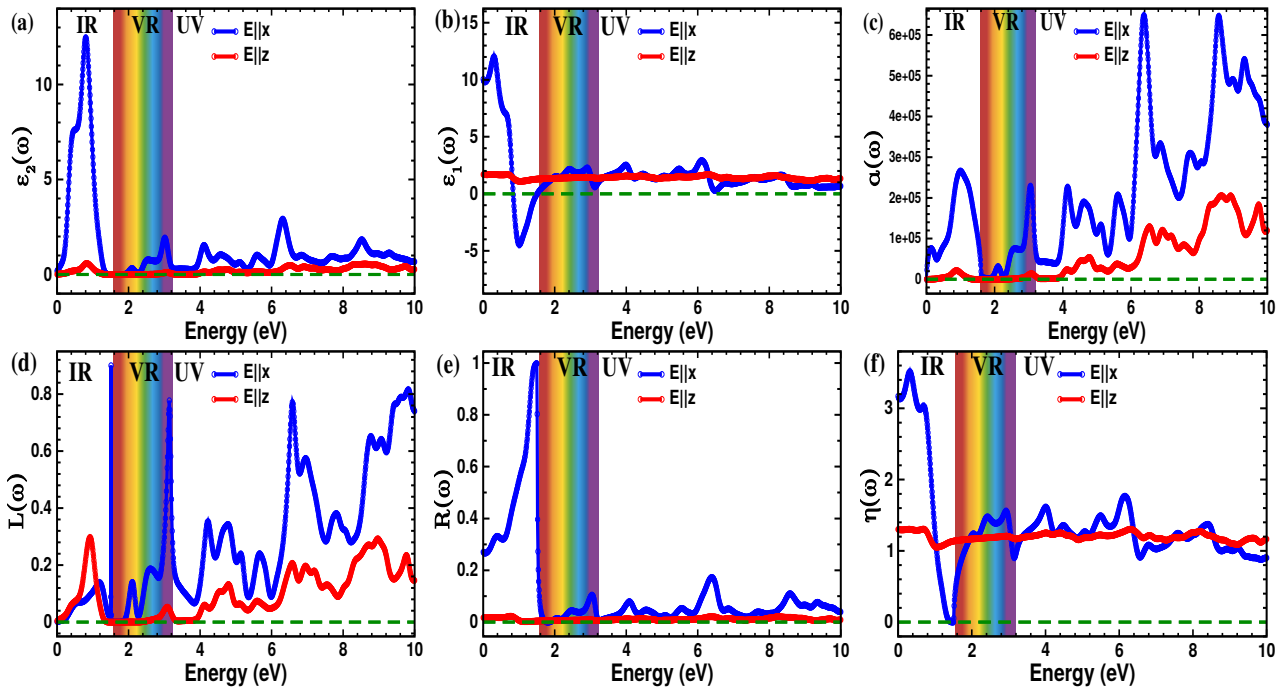

Figure 8: (Color online) (a) Imaginary part of dielectric function, (b) real part of dielectric function, (c) absorption coefficient, (d) energy loss function, (e) reflectivity, and (f) refractive index, as a function of photon energy. Blue and red solid curves represent in-plane and out-of-plane incident light in p-SiCN monolayer, respectively.

optical anisotropy in p-SiCN which is due to the differences in exposed geometry.

The predominat peaks of the real $\varepsilon_1(\omega)$ and imaginary $\varepsilon_2(\omega)$ part of the dielectric function (Figure 8a-b) shows relatively stronger optical response of p-SiCN in IR and UV region with obvious red shifts for E||x. The peaks of $\varepsilon_2(\omega)$ demonstrates the inter-band transition essentially due to 3p-orbitals of Si, C, N and 2p of Si depicted in PDOS (Figure 7). Meanwhile the $\varepsilon_1(\omega)$ is related to the energy stored by the medium when a material is exposed. In particular, $\varepsilon_1(\omega)$ at 0 eV describes the static dielectric constant $\varepsilon_1(0)$ with a value of 10.01, which is higher than that of p-graphene[43] and other well-known 2D materials for E||x[44]. Most importantly, the negative value of $\varepsilon_1(\omega)$ in between the range of 0.85 -1.50 eV for E||x indicates the plasma frequency, crucial in plasmonics[45,46].

Similarly, the absorption coefficient, $\alpha(\omega)$, (Figure 8c)is calculated to investigate the optical absorption of this metallic monolayer. The absorption increases exponentially in the infrared region (IR) followed by a gradual drop and growth in the visible region (VR) and Ultraviolet (UV) region, respectively. This indicates that the monolayer relatively does not absorb proper visible light. The maximum absorption is at 6.38 eV ($\approx 6.51\times10^5$ cm^{-1}) in the E||x direction, which is higher than that of p-BCN structure, including penta-graphene[43] and some other well-known 2D materials[44,47] for the E||x. A similar trend is observed in the optical energy loss spectrum (Figure 8d), except for the abrupt growth of loss at 1.5 eV in E||x, which is linked with the plasmon frequency[48]. In addition, the loss is comparatively higher for E||z orientation in the IR region. This justifies the cause of reduced optical spectra for p-SiCN in the out-of-plane direction.

Similarly, the reflectivity is relatively higher (99% at 1.5 eV) in the E||x (Figure 8e), especially in IR. The lower reflectivity intensity in the VR indicates that the p-SiCN is almost transparent for visible light. In addition, the refractive index, $\eta(\omega)$, (Figure 8f) identifies the nature of light propagation. In particular, at zero photon energy, it gives the static refractive index, $\eta(0)$, of 3.17 (E||x) and 1.30 (E||z),

which are higher than those of p-BCN (1.43) and penta-graphene (1.62)[49]. Remarkably, zero refractive index is detected at ≈1.50 eV for E||z which is due to strong dispersion of the surface plasma on the material[50]. These result establishes that p-SiCN is an optical meta-meterial with enormous potential applications in topological photonics[51].

These optical findings reveal that the optical spectra are predominant in IR and UV mostly in the E||x orientation and with the possibility to be used in IR and UV regions operated device applications. The high anisotropy, significant optical absorption, and small reflectance, in particular, offer the opportunity to develop and test high-quality optical waveguides, polarizers, energy harvesters, and photovoltaic applications.

CONCLUSIONS

In summary, we theoretically discovered the p-SiCN monolayer, whose stability and experimental feasibility are verified by investigating the thermal, mechanical, and dynamical sustainability. The p-SiCN is a ternary 2D metallic mechanical metamaterial with non-trivial geometrical and mechanical isotropy. Remarkably, the shorter and quasi sp^3-hybridized C−N bond and the rigidity against the strain allows the monolayer to possess a high value of negative Poisson's ratio (-0.136), even higher than the black phosphorene, extendable up to -0.639 by 4% of biaxial stretching. Additionally, the pronounced reduction in 2D Young's modulus from 129.88 N/m to 41.34 N/m at equivalent stretching reflects its relative softening − an important metric for flexible and stretchable devices. Interestingly, the buckled−to− planar phase transition is identified at 10% biaxial strain before it suffers the fracture at 16%. In addition, the strong optical anisotropy, absorbance (up to 6.51×10^5 cm^{-1}), and presence of plasmon frequency demonstrate its an application in optomechanical and plasmonics. Hence, p-SiCN is an exceptional material for the applications of nano-auxetics, nanomechanical and optomechanical devices. These intriguing properties and the untold number of applications demand urgent experimental validation and deployment.

COMPUTATIONAL METHODS

The Spanish Initiative for Electronic Simulations with Thousands of Atoms (SIESTA)[52,53] with the semi-local form of norm-conserving pseudopotentials[54] is used for the density functional theory (DFT) calculations. The generalized gradient approximation (GGA) of Perdew-Burke-Ernzerhof (PBE)[55] is used within the double zeta plus polarization (DZP) basis sets. The k-points of 20×20×1 within Monkhrost pack scheme[56] and 350 Rydberg cutoff energy meet the convergence criteria. The atomic force of 0.02 eV/Å and self-consistent field of 10^{-6} eV are set for tight convergence within the conjugate-gradient (CG) scheme. A vertical separation of 25 Å is used along the z−axis to avoid unnecessary interlayer interactions. The chemical stability is tested by analyzing formation (E_f)[29] and cohesive (E_{coh})[57] energies. The dynamical stability of the penta-SiCN is ensured by calculating phonon spectra from the finite displacement method implemented in the PHONOPY package[58]. The force constants to build the required dynamical matrix are obtained from the sets of forces calculated using the Viena Ab-initio Simulation Package (VASP)[59]. Furthermore, we performed the ab-initio molecular dynamics (AIMD) simulations to account for the thermal stability. In both phonon and AIMD calculations, 4×4×1 supercell is used to the convergence. The Young's modulus (Y) and Poisson's ratio (ν) as functions of the direction angle θ are represented by the relations:[38]

$$Y(\theta) = \frac{C_{11}C_{22} - C_{12}^2}{C_{22}\cos^4(\theta) + A\cos^2(\theta)\sin^2(\theta) + C_{11}\cos^4(\theta)}$$

$$\nu(\theta) = \frac{C_{12}\cos^4(\theta) - B\cos^2(\theta)\sin^2(\theta) + C_{12}\cos^4(\theta)}{C_{22}\cos^4(\theta) + A\cos^2(\theta)\sin^2(\theta) + C_{11}\cos^4(\theta)}$$

where $A = (C_{11}C_{22} - C_{12}^2)/C_{66} - 2C_{12}$ and $B = C_{11} + C_{22} - (C_{11}C_{22} - C_{12}^2)/C_{66}$.

To perform optical calculations with SIESTA, a 60×60×1 k-mesh within the Monkhorst-Pack

scheme and an optical broadening of 0.1 eV is used. SIESTA implements the first order time dependent perturbation theory (TDP)[60]. The dielectric function $\varepsilon(\omega)$ can be expressed as:

$$\varepsilon(\omega) = \varepsilon_1(\omega) + i\varepsilon_2(\omega), \tag{1}$$

where $\varepsilon_1(\omega)$ is the real part of the dielectric function, and is obtained using the Kramer-Kronig transformation (KK) of $\varepsilon_2(\omega)$ and is expressed as:

$$\varepsilon_1(\omega) = 1 + \frac{2}{\pi} P \int_0^\infty \frac{\varepsilon_2(\omega')\,\omega'}{\omega'^2 - \omega^2} d\omega', \tag{2}$$

where P denotes the principle part of $\varepsilon_1(\omega)$[61].

On the other hand, $\varepsilon_2(\omega)$ is the imaginary part of $\varepsilon(\omega)$, and can be obtained with the help of TDP as:

$$\varepsilon_2(\omega) = \frac{e^2}{\omega^2 \pi m^2} \sum_{v,c} \int_{BZ} d\vec{k} \left|\langle \psi_{ck} | \hat{e} \cdot \vec{p} | \psi_{vk} \rangle\right|^2 \delta\left(E_c(k) - E_v(k) - \hbar\omega\right). \tag{3}$$

Equation (3) elucidates the dependencies between the electronic and optical behavior. Here, v and c indicate the valence and the conduction band states, respectively. $E_{(c,v)}(k)$ and $\psi_{(c,v),k}$ are the corresponding energy and eigenfunction of these states. $\vec{p}$ and $\hat{e}$ are the momentum operator and polarization vector, respectively. Further, the complex refractive index (N) is expressed as $N = \sqrt{\varepsilon(\omega)} = \eta(\omega) + iK(\omega)$, where $\eta(\omega)$ and $K(\omega)$ are the refractive index and extinction coefficient, respectively. These parameters are expressed as:

$$\eta(\omega) = \left(\frac{\sqrt{\varepsilon_1^2(\omega) + \varepsilon_2^2(\omega)} + \varepsilon_1(\omega)}{2} \right)^{\frac{1}{2}} \tag{4}$$

$$K(\omega) = \left(\frac{\sqrt{\varepsilon_1^2(\omega) + \varepsilon_2^2(\omega)} - \varepsilon_1(\omega)}{2} \right)^{\frac{1}{2}}. \tag{5}$$

Furthermore, the reflectivity R(ω) and absorption coefficient $\alpha(\omega)$ are expressed as[62]:

$$R(\omega) = \frac{K^2(\omega) + [1 - n(\omega)]^2}{K^2(\omega) + [1 + n(\omega)]^2}. \tag{6}$$

$$\alpha(\omega) = \frac{2\omega K(\omega)}{c}. \tag{7}$$

Additionally, the electron energy loss function L(ω) is given by the relation $L(\omega) = \mathrm{Im}\left(-\frac{1}{\varepsilon(\omega)}\right)$, and can also be expressed in terms of $\varepsilon_1(\omega)$ and $\varepsilon_2(\omega)$ as:

$$L(\omega) = \frac{\varepsilon_2(\omega)}{\varepsilon_1^2(\omega) + \varepsilon_2^2(\omega)}. \tag{8}$$

All these optical parameters are calculated in the interval between 0 to 20 eV for parallel (E$\|$x) and perpendicular (E||z) polarization of electric field.

Acknowledgement The authors acknowledge the financial and technical support provided by Khalifa University of Science and Technology (KU) under project No. CIRA-2019-037, and KU-HPC facility. D.P. acknowledges the support provided by Ames Laboratory (US-DOE) under its contract with Iowa State University, Contract No. DE-AC02-07CH11358. We are thankful to Dr. Rajendra Adhikari (Kathmandu University Supercomputer Center) for his technical assistance.

References

(1) Zhang, S.; Zhou, J.; Wang, Q.; Chen, X.; Kawazoe, Y.; Jena, P. Penta-graphene: A new carbon allotrope. *PNAS* **2015**, *112*, 2372–2377.

(2) Prévot, G.; Hogan, C.; Leoni, T.; Bernard, R.; Moyen, E.; Masson, L. Si nanoribbons on Ag (110) studied by grazing-incidence x-ray diffraction, scanning tunneling microscopy, and density-functional theory: evidence of a pentamer chain structure. *Phys. Rev. Lett.* **2016**, *117*, 276102.

(3) Sheng, S.; Ma, R.; Wu, J.-b.; Li, W.; Kong, L.; Cong, X.; Cao, D.; Hu, W.; Gou, J.; Luo, J.-W. The pentagonal nature of self-assembled silicon chains and magic clusters on Ag (110). *Nano Lett.* **2018**, *18*, 2937–2942.

(4) Cerdá, J. I.; Sławińska, J.; Le Lay, G.; Marele, A. C.; Gómez-Rodríguez, J. M.; Dávila, M. E. Unveiling the pentagonal nature of perfectly aligned single- and double-strand Si nano-ribbons on Ag (110). *Nat. Commun.* **2016**, *7*, 1–7.

(5) Chow, W. L.; Yu, P.; Liu, F.; Hong, J.; Wang, X.; Zeng, Q.; Hsu, C.-H.; Zhu, C.; Zhou, J.; Wang, X. High mobility 2D palladium diselenide field-effect transistors with tunable ambipolar characteristics. *Adv.* **2017**, *29*, 1602969.

(6) Alderson, A.; Alderson, K. Auxetic materials. *Proc Inst Mech Eng G J Aerosp Eng.* **2007**, *221*, 565–575.

(7) Yang, W.; Li, Z.-M.; Shi, W.; Xie, B.-H.; Yang, M.-B. Review on auxetic materials. *J. Mater. Sci.* **2004**, *39*, 3269–3279.

(8) Li, X.; Qiang, X.; Gong, Z.; Zhang, Y.; Gong, P.; Chen, L. Tunable Negative Poissons Ratio in Van der Waals Superlattice. *Res* **2021**, *2021*, 1904839.

(9) Huang, C.; Chen, L. Negative Poisson's ratio in modern functional materials. *Adv.* **2016**, *28*, 8079–8096.

(10) Choi, J.; Lakes, R. Design of a fastener based on negative Poisson's ratio foam. *Cell. Polym.* **1991**, *10*, 205–212.

(11) Avellaneda, M.; Swart, P. J. Calculating the performance of 1–3 piezoelectric composites for hydrophone applications: an effective medium approach. *J. Acoust. Soc. Am* **1998**, *103*, 1449–1467.

(12) Lakes, R. Foam structures with a negative Poisson's ratio. *Science* **1987**, *235*, 1038–1040.

(13) Greaves, G. N.; Greer, A. L.; Lakes, R. S.; Rouxel, T. Poisson's ratio and modern materials. *Nat. Mater.* **2011**, *10*, 823–837.

(14) Scarpa, F. Auxetic materials for bioprostheses [In the Spotlight]. *IEEE Signal Process. Mag* **2008**, *25*, 128–126.

(15) Kong, X.; Deng, J.; Li, L.; Liu, Y.; Ding, X.; Sun, J.; Liu, J. Z. Tunable auxetic properties in group-IV monochalcogenide monolayers. *Phys. Rev. B* **2018**, *98*, 184104.

(16) Jiang, J.-W.; Park, H. S. Negative poissons ratio in single-layer black phosphorus. *Nat. Commun.* **2014**, *5*, 1–7.

(17) Peng, R.; Ma, Y.; Wu, Q.; Huang, B.; Dai, Y. Two-dimensional materials with intrinsic auxeticity: progress and perspectives. *Nanoscale* **2019**, *11*, 11413–11428.

(18) Kou, L.; Ma, Y.; Tang, C.; Sun, Z.; Du, A.; Chen, C. Auxetic and ferroelastic borophane: a novel 2D material with negative Possions ratio and switchable dirac transport channels. *Nano Lett.* **2016**, *16*, 7910–7914.

(19) Han, J.; Xie, J.; Zhang, Z.; Yang, D.; Si, M.; Xue, D. Negative Poissons ratios in few-layer orthorhombic arsenic: First-principles calculations. *Appl. Phys. Express* **2015**, *8*, 041801.

(20) Zhou, L.; Zhuo, Z.; Kou, L.; Du, A.; Tretiak, S. Computational dissection of two-dimensional rectangular titanium mononitride TiN: auxetics and promises for photocatalysis. *Nano Lett.* **2017**, *17*, 4466–4472.

(21) Wang, Y.; Li, F.; Li, Y.; Chen, Z. Semimetallic Be 5 C 2 monolayer global minimum with quasi-planar pentacoordinate carbons and negative Poissons ratio. *Nat. Commun.* **2016**, *7*, 1–7.

(22) Wang, Y.; Li, F.; Li, Y.; Chen, Z. Semimetallic Be 5 C 2 monolayer global minimum with quasi-planar pentacoordinate carbons and negative Poissons ratio. *Nat. Commun.* **2016**, *7*, 1–7.

(23) Yagmurcukardes, M.; Sahin, H.; Kang, J.; Torun, E.; Peeters, F. M.; Senger, R. T. Pentagonal monolayer crystals of carbon, boron nitride, and silver azide. *J. Appl. Phys.* **2015**, *118*, 104303.

(24) Liu, G.; Zeng, Q.; Zhu, P.; Quhe, R.; Lu, P. Negative Poisson's ratio in monolayer PdSe2. *Comput. Mater. Sci.* **2019**, *160*, 309–314.

(25) Oyedele, A. D.; Yang, S.; Liang, L.; Puretzky, A. A.; Wang, K.; Zhang, J.; Yu, P.; Pudasaini, P. R.; Ghosh, A. W.; Liu, Z. PdSe2: pentagonal two-dimensional layers with high air stability for electronics. *J. Am. Chem. Soc.* **2017**, *139*, 14090–14097.

(26) Guo, Y.; Zhou, J.; Xie, H.; Chen, Y.; Wang, Q. Screening transition metal-based polar pentagonal monolayers with large piezoelectricity and shift current. *Npj Comput. Mater.* **2022**, *8*, 1–9.

(27) Chen, Q.-Y.; Liu, M.-y.; Cao, C.; He, Y. Anisotropic optical properties induced by uniaxial strain of monolayer C 3 N: a first-principles study. *RSC Adv.* **2019**, *9*, 13133–13144.

(28) Liu, S.; Liu, B.; Shi, X.; Lv, J.; Niu, S.; Yao, M.; Li, Q.; Liu, R.; Cui, T.; Liu, B. Two-dimensional penta-BP 5 sheets: High-stability, strain-tunable electronic structure and excellent mechanical properties. *Sci. Rep.* **2017**, *7*, 1–8.

(29) Zhang, S.; Zhou, J.; Wang, Q.; Jena, P. Beyond graphitic carbon nitride: nitrogen-rich penta-CN2 sheet. *J. Phys. Chem* **2016**, *120*, 3993–3998.

(30) Marianetti, C. A.; Yevick, H. G. Failure mechanisms of graphene under tension. *Phys. Rev. Lett.* **2010**, *105*, 245502.

(31) Si, C.; Duan, W.; Liu, Z.; Liu, F. Electronic strengthening of graphene by charge doping. *Phys. Rev. Lett.* **2012**, *109*, 226802.

(32) Zhao, K.; Guo, Y.; Shen, Y.; Wang, Q.; Kawazoe, Y.; Jena, P. Penta-BCN: A new ternary pentagonal monolayer with intrinsic piezoelectricity. *J. Phys. Chem* **2020**, *11*, 3501–3506.

(33) Born, M.; Misra, R. D. On the stability of crystal lattices. IV. Mathematical Proceedings of the Cambridge Philosophical Society. 1940; pp 466–478.

(34) Wang, B.; Wu, Q.; Zhang, Y.; Ma, L.; Wang, J. Auxetic B4N monolayer: a promising 2D material with in-plane negative Poissons ratio and large anisotropic mechanics. *ACS Appl. Mater. Interfaces* **2019**, *11*, 33231–33237.

(35) Sharma, S. B.; Bhatta, R.; Adhikari, R.; Paudyal, D. Strain dependent electronic and optical responses of penta-BCN monolayer. *Carbon Trends* **2022**, 100162.

(36) Dabsamut, K.; Thanasarnsurapong, T.; Maluangnont, T.; Jiraroj, T.; Jungthawan, S.; Boonchun, A. Strain engineering and thermal conductivity of a penta-BCN monolayer: a computational study. *J. Phys* **2021**,

(37) Sun, W.; Shen, Y.; Guo, Y.; Chen, Y.; Wang, Q. 1, 2, 4-Azadiphosphole-based piezoelectric penta-CNP sheet with high spontaneous polarization. *Appl. Surf. Sci.* **2021**, *554*, 149499.

(38) Chen, S.-B.; Zeng, Z.-Y.; Chen, X.-R.; Yao, X.-X. Strain-induced electronic structures, mechanical anisotropy, and piezoelectricity of transition-metal dichalcogenide monolayer CrS2. *J. Appl. Phys.* **2020**, *128*, 125111.

(39) Li, F.; Tu, K.; Zhang, H.; Chen, Z. Flexible structural and electronic properties of a pentagonal B 2 C monolayer via external strain: a computational investigation. *Phys. Chem. Chem. Phys.* **2015**, *17*, 24151–24156.

(40) Zhang, T.; Ma, Y.; Huang, B.; Dai, Y. Two-dimensional penta-BN2 with high specific capacity for Li-ion batteries. *ACS Appl. Mater. Interfaces* **2019**, *11*, 6104–6110.

(41) Ljungberg, M. P.; Vänskä, O.; Koval, P.; Koch, S.; Kira, M.; Sánchez-Portal, D.

Charge-transfer states and optical transitions at the pentacene-TiO2 interface. *New J. Phys.* **2017**, *19*, 033019.

(42) Nayebi, P.; Emami-Razavi, M.; Zaminpayma, E. Study of electronic and optical properties of CuInSe2 nanowires. *J. Phys. Chem* **2016**, *120*, 4589–4595.

(43) Dai, X.; Shen, T.; Feng, Y.; Liu, H. Structure, electronic and optical properties of Al, Si, P doped penta-graphene: A first-principles study. *Phys. B: Condens. Matter* **2019**, *574*, 411660.

(44) John, R.; Merlin, B. Optical properties of graphene, silicene, germanene, and stanene from IR to far UV–A first principles study. *J Phys Chem Solids* **2017**, *110*, 307–315.

(45) West, P. R.; Ishii, S.; Naik, G. V.; Emani, N. K.; Shalaev, V. M.; Boltasseva, A. Searching for better plasmonic materials. *Laser Photon Rev* **2010**, *4*, 795–808.

(46) Guan, S.; Yang, S. A.; Zhu, L.; Hu, J.; Yao, Y. Electronic, Dielectric and Plasmonic Properties of Two-Dimensional Electride Materials X2N (X= Ca, Sr): A First-Principles Study. *Sci. Rep.* **2015**, *5*, 1–14.

(47) Laturia, A.; Van de Put, M. L.; Vandenberghe, W. G. Dielectric properties of hexagonal boron nitride and transition metal dichalcogenides: from monolayer to bulk. *NPJ 2D Mater. Appl* **2018**, *2*, 1–7.

(48) Ding, Z.; Peng, J.; Xie, X.; Hu, J.; Yang, H.; Wu, F.; Dong, H. Optical characteristic study of monolayer VS2 based on first-principles calculations. *Solid State Commun.* **2017**, *266*, 26–29.

(49) Wang, Z.; Dong, F.; Shen, B.; Zhang, R.; Zheng, Y.; Chen, L.; Wang, S.; Wang, C.; Ho, K.; Fan, Y.-J. Electronic and optical properties of novel carbon allotropes. *Carbon* **2016**, *101*, 77–85.

(50) Ding, Z.; Peng, J.; Xie, X.; Hu, J.; Yang, H.; Wu, F.; Dong, H. Optical characteristic study of monolayer VS2 based on first-principles calculations. *Solid State Commun.* **2017**, *266*, 26–29.

(51) Horsley, S.; Woolley, M. Zero-refractive-index materials and topological photonics. *Nat. Phys* **2021**, *17*, 348–355.

(52) Soler, J. M.; Artacho, E.; Gale, J. D.; García, A.; Junquera, J.; Ordejón, P.; Sánchez-Portal, D. The SIESTA method for ab initio order-N materials simulation. *J. Condens. Matter Phys.* **2002**, *14*, 2745.

(53) Artacho, E.; Sánchez-Portal, D.; Ordejón, P.; Garcia, A.; Soler, J. M. Linear-scaling ab-initio calculations for large and complex systems. *Phys. Status Solidi B* **1999**, *215*, 809–817.

(54) Troullier, N.; Martins, J. L. Efficient pseudopotentials for plane-wave calculations. *Phys. Rev. B* **1991**, *43*, 1993.

(55) Perdew, J. P.; Burke, K.; Ernzerhof, M. Generalized gradient approximation made simple. *Phys. Rev. Lett.* **1996**, *77*, 3865.

(56) Monkhorst, H. J.; Pack, J. D. Special points for Brillouin-zone integrations. *Phys. Rev. B* **1976**, *13*, 5188.

(57) Noor-A-Alam, M.; Kim, H. J.; Shin, Y.-H. Dipolar polarization and piezoelectricity of a hexagonal boron nitride sheet decorated with hydrogen and fluorine. *Phys. Chem. Chem. Phys.* **2014**, *16*, 6575–6582.

(58) Togo, A.; Oba, F.; Tanaka, I. First-principles calculations of the ferroelastic transition between rutile-type and CaCl 2-type SiO 2 at high pressures. *Phys. Rev. B* **2008**, *78*, 134106.

(59) Kresse, G.; Joubert, D. Phys Rev B Condens Matter Mater Phys 59: 1758 https://doi. org/10.1103. 1999.

(60) Saha, S.; Sinha, T.; Mookerjee, A. Electronic structure, chemical bonding, and

optical properties of paraelectric BaTiO 3. *Phys. Rev. B* **2000**, *62*, 8828.

(61) Fadaie, M.; Shahtahmassebi, N.; Roknabad, M.; Gulseren, O. Investigation of new two-dimensional materials derived from stanene. *Comput. Mater. Sci.* **2017**, *137*, 208–214.

(62) Mohebpour, M. A.; Vishkayi, S. I.; Tagani, M. B. Tuning electronic and optical properties of free-standing Sn2Bi monolayer stabilized by hydrogenation. *J. Appl. Phys.* **2020**, *127*, 014302.